Predictive modeling of fracture behavior in Ti6Al4V alloys manufactured by SLM process

Mohsen Sarparast
Department of Mechanical, Industrial & Manufacturing Engineering, The University of Toledo, Toledo, OH, USA
Mohsen.Sarparast@rockets.utoledo.edu, https://orcid.org/0000-0002-9159-8460

Majid Shafaie
Department of Mechanical Engineering, Amirkabir University of Technology, Tehran, Iran.
magician754@aut.ac.ir, https://orcid.org/0000-0002-3140-5495

Mohammad Davoodi, Ahmad Memaran Babakan
Department of Mechanical Engineering, K. N. Toosi University of Technology, Tehran, Iran.
m.e_davoodi@yahoo.com, ahmadmemaran1991@gmail.com

Hongyan Zhang
Department of Mechanical, Industrial & Manufacturing Engineering, The University of Toledo, Toledo, OH, USA
hongyan.zhang@utoledo.edu

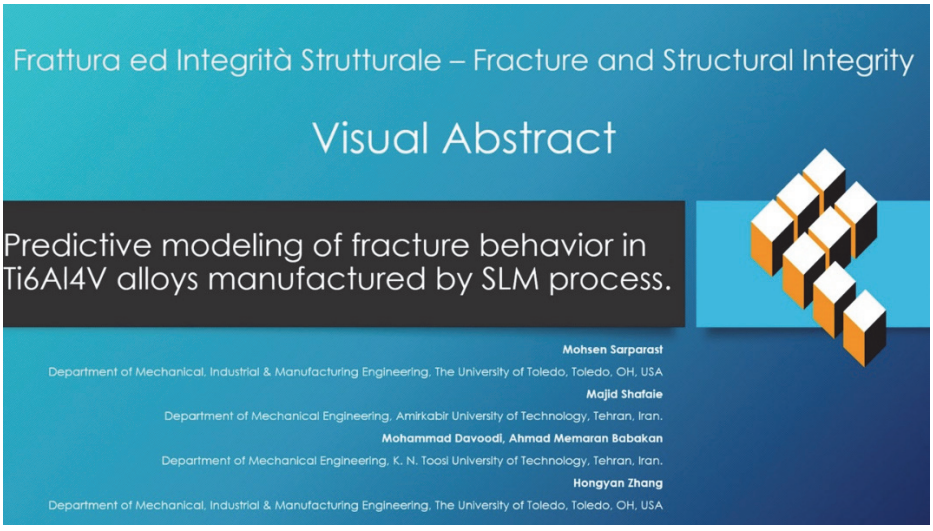

Citation: Sarparast, M., Shafaie, M., Davoodi, M., Memaran Babakan, A., Zhang, H., Predictive modeling of fracture behavior in Ti6Al4V alloys manufactured by SLM process, Frattura ed Integrità Strutturale, 68 (2024) 340-356.

Received: 29.12.2024
Accepted: 09.03.2024
Published: 10.03.2024
Issue: 04.2024

KEYWORDS. Fracture, GTN model, AM, ANN, Hidden layers.

INTRODUCTION

Additive manufacturing (AM) is a powerful technique in digital-manufacturing objects from three-dimensional (3D) models by depositing materials layer by layer. Complex structures that are difficult to be produced through traditional manufacturing processes can be easily fabricated by AM processes [1-5].

The selective laser melting (SLM) is a widely used additive manufacturing (AM) process for producing metallic components, particularly when utilizing powder-based materials. Its versatility has garnered attention from various industries, including biomedical and aerospace sectors. Ti6Al4V, a titanium alloy, is particularly popular for the SLM process due to its exceptional properties, such as high strength-to-weight ratio, low density, high fracture toughness, excellent corrosion resistance, and remarkable biocompatibility. These characteristics make Ti6Al4V ideal for manufacturing final parts through the SLM process [6-10].

The study of fracture behavior in additively manufactured components is a common topic among scientists due to the complex stress and damage exposure these components endure. Numerous researchers have dedicated their efforts to investigate and evaluate the fracture behavior of additively manufactured components, employing a combination of computational modeling and experimental analysis. In these studies, micromechanical models have been developed to capture the intricate nature of ductile fracture, considering processes such as micro-void nucleation, growth, and coalescence [11]. However, the findings from these investigations have often yielded varying results, highlighting the complexity of the fracture behavior in additively manufactured components and the need for further research and analysis [12-16]. In micromechanical modeling, Gurson [17] developed a significant contribution by introducing a model that predicts material behavior based on the growth of spherical cavities. Then, Tvergaard and Needleman [18] made further advancements by modifying the Gurson model to incorporate void coalescence and a constitutive model via the dependence of the yield function on the void volume fraction (GTN modified model). Alexander et al. [19] studied the fracture behavior of SLM additively manufactured Ti-6AL-4V alloy in an experimental and computational modeling investigation and observed that combined triaxiality and lode angle parameters have more accuracy in contrast to no stress state-dependence. To enhance the precision of fracture property prediction using the GTN fracture model, calibration of certain coefficients is essential, typically through experimental testing. However, this calibration process can be time-consuming and requires specialized equipment, often involving a trial-and-error approach [20, 21]. The (ANN) models have emerged as powerful tools for information processing, learning, and problem-solving in this context [22, 23]. ANN models possess the capability to predict network boundaries and identify complex relationships among various parameters. By leveraging the strengths of ANN models, the process can be refined and fine-tuned, ultimately leading to improved efficiency, reduced defects, and enhanced quality in digital fabrication [24-29].

Numerous scientists have recognized the potential of the ANN models in AM to save time and streamline the optimization of process parameters. By training an ANN model, researchers can leverage its computational power to efficiently explore and identify optimal machine settings for the fabrication process [7, 29]. Wang et al. [30] observed that ANN serve as effective assistants in optimizing process parameters and defect monitoring. Their research demonstrated the capability of ANN models to analyze complex relationships and provide valuable insights for process optimization and defect detection. In another related study, Chinchanikar et al. [31] utilized ANN to predict the surface roughness of parts manufactured using fused deposition modeling (FDM) based on process parameters. They employed machine learning algorithms to model the ANN and evaluated its prediction accuracy. Their findings indicated that ANN models with two hidden layers consisting of 150 neurons performed better in prediction accuracy than models with a single hidden layer containing 250 neurons. Mehrpouya et al. [32] conducted two studies using ANN to investigate the effect of process parameters on various aspects of AM, such as mechanical properties, density, and temperature transformation. They developed a prediction model using ANN to optimize the manufacturing parameters for NiTi alloy. In the study conducted by Kowen et al. [23], the focus was on assessing the quality of printed parts in the SLM process. They employed the ANN to investigate the relationship between laser power and its impact on forming of cracks and pores in the printed parts. The ANN model was utilized to analyze the complex interactions between laser power and the occurrence of defects, providing insights into optimizing the SLM process to minimize crack and pore formation. Also, Stathatos et al [16] employed ANN in a laser-based AM process. Their objective was to predict the temperature evolution and density of the fabricated parts. The ANN model was trained using data collected during the AM process, allowing for accurate predictions of temperature profiles and density variations throughout the fabrication process. Jimenez [33] utilized ANN to analysis of fatigue life in nodular cast iron. By incorporating synthetic data as complementary input data, the ANN model was able to effectively enhance its forecasting capabilities. This approach

enabled more accurate predictions of nodular cast iron fatigue life, contributing to improved understanding and optimization of the material's performance applications [34].

This study investigates the influence of the number of neurons and hidden layers on the accuracy of forecasting parameters in the GTN fracture model using ANNs. The research focuses on predicting the complex relationships between input and output data within the GTN fracture model for SLM-fabricated parts made of Ti6Al4V alloy. By training the ANN with various configurations of hidden layers and neurons, the study investigates how these architectural choices impact the accuracy of parameter forecasting in the GTN fracture model. This analysis provides valuable insights into the optimal setup for achieving precise predictions of fracture behavior in SLM-fabricated Ti6Al4V alloy components. Fig. 1 illustrates the methodology employed in this study. Moreover, the relative importance of each input variable was determined by analyzing the calibrated connection weights. This analysis involved assessing the contribution of each input variable by considering their respective connection weights within the neural network. By examining these calibrated connection weights, we could evaluate and quantify each input variable's relative importance in influencing the neural network's output or behavior.

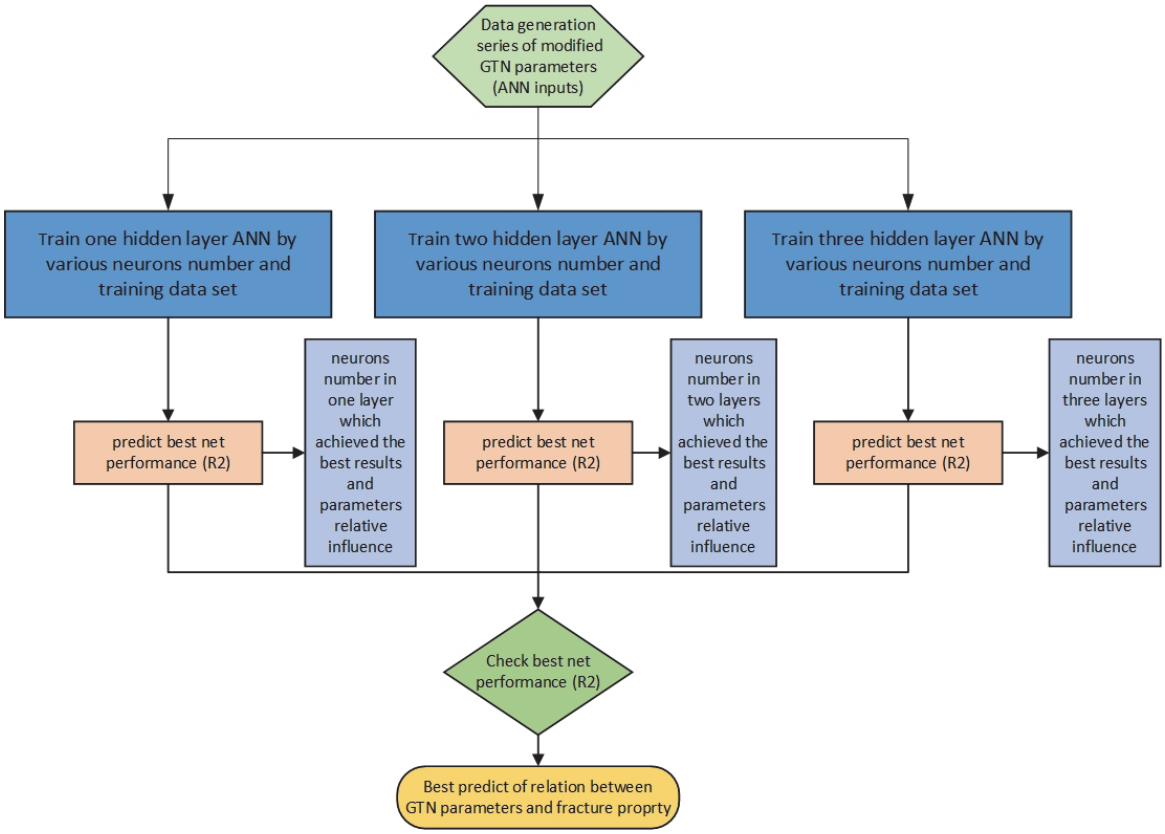

Figure 1: The graphical representation of the methodology.

SPECIMENS PREPARATION

In this study, Ti-6Al-4V alloy specimens were fabricated using the SLM additive manufacturing process, following the guidelines specified in the ASTM F2924 standard [35]. The Ti-6Al-4V alloy specimens utilized in the experimental investigation were fabricated using the NOURA.CO M100p machine. The chemical compositions of the Ti-6Al-4V Powder, as outlined in Tab. 1, were employed for this purpose. The specific parameters and settings used during the manufacturing process are provided in Tab. 2. Also, tensile specimens were prepared by applying black dots to white-painted surfaces for digital image correlation (DIC) Method. By this method the first image is utilized as a reference for the zero-load condition, and a defined area of interest is used to calculate strain, primarily in the vertical direction. This thorough procedure allows for the assessment of material deformation and strain behavior during tensile testing[36].

The specimens were subjected to a heat treatment process conducted in an Argon environment for 3 hours at a temperature of 650 °C. Fig. 2 illustrates the printed specimens obtained through the SLM process.

Element	Al	V	Fe	C	H	O	N	Ti
Wt (%)	5.5 ˜ 6.75	3.5 ˜4.5	< 0.30	< 0.08	< 0.015	<0.20	<0.05	rest

Table 1: The chemical compositions of the Ti-6Al-4V powder.

Parameters	Value
Laser power (W)	280
Scanning speed (mm/s)	800
Hatch spacing (μm)	140
Layer height (μm)	60

Table 2: Process parameters for fabrication of the specimens.

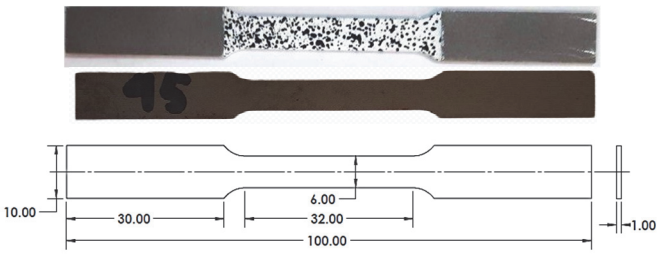

Figure 2: Uniaxial test specimen and prepared specimen for digital image correlation (DIC).

TENSION TEST

To assess the mechanical properties of SLM-printed Ti-6Al-4V alloy components, we conducted tensile tests using the SANTAM STM150 testing machine. The tests were conducted with a loading speed of approximately 0.3 mm/min [37], as shown in Fig. 3. These tests aimed to evaluate the material's response to uniaxial tension and extract its mechanical properties [28, 38, 39]. Also, images of tensile test for the specimens were acquired at 5-second intervals using a high-resolution camera throughout the test. The strain magnitude was determined using a DIC system. The Ncorr function [36], which is a component of the MATLAB software [40], was employed for the purpose of image analysis. Tab. 3 presents the mechanical properties of the additive-manufactured Ti-6Al-4V alloys obtained from the uniaxial tension tests. These properties provide valuable information about the material's elastic and plastic behavior under applied stress. The experimental results for maximum force and fracture displacement are 5768.3 N and 0.40 mm, respectively. The Voce hardening law was employed to describe the material's hardening behavior. The Voce hardening law is a mathematical model that characterizes the material's strengthening response as a function of plastic strain. By considering the Voce hardening law, the researchers aimed to accurately capture the material's hardening behavior during deformation [41].

$$\sigma_f = B - (B - A).e^{-m*(\varepsilon_0 + \varepsilon^p)} \quad (1)$$

where A, B, m, and ε_0 are Voce hardening law coefficients.

Property	Value
Density (kg/m^3)	4800
Young's modulus (MPa)	105000
Poisson's ratio	0.342
Initial yield stress (MPa)	920
UTS (MPa)	987
A	985
B	-30
m	302
ε_0	0.009

Table 3: Mechanical properties of Ti–6Al–4V AM sheets.

Figure 3: Machine setup for the tensile test [42].

FINITE ELEMENT SIMULATION

This study utilizes the VUMAT user subroutine in FE commercial software Abaqus to conduct finite element simulations and MATLAB software to calibrate GTN fracture model [22, 43, 44]. To facilitate this process, a Python [45] script within Abaqus developed and linked with MATLAB software to develop ANN [40].

Fig. 4 shows eight-node solid elements with reduced integration (C3D8R) are chosen for the finite element simulation model. These elements are suitable for accurately representing the structural response and capturing the relevant material behavior. A local element size of 0.2 mm is chosen specifically in the critical necking area where crack initiation is likely to occur to ensure an accurate examination of deformation outcomes[46]. This reduced element size enables a comprehensive analysis of the deformation characteristics within this particular region. The total number of elements in the model is 49,400, while the number of nodes is 61,074.

The GTN fracture model, initially proposed by Gurson and subsequently modified by Tvergaard and Needleman, has been widely utilized in the field of ductile and plasticity mechanics for characterizing the fracture behavior and damage

progression of metallic materials [17, 41, 47, 48]. However, the GTN model has limitations in accurately capturing void shear failure under low and negative-stress triaxiality conditions. To address this limitation, Nashon and Hutchison proposed enhancing the GTN fracture model by incorporating coefficients for void coalescence, nucleation, and shear damage. These modifications improve the model's capability to accurately represent the fracture behavior of metallic materials, particularly in scenarios involving low and negative-stress triaxiality. The modified GTN fracture model by Nashon and Hutchison provides researchers with a more comprehensive tool for analyzing and predicting the response of materials under complex loading conditions, thereby facilitating improved understanding and design of structures and components in diverse engineering applications[49].

$$\Phi = \frac{q^2}{\sigma_y^{\ 2}} + 2q_1 f^* \cosh\left(-\frac{3q_2 P}{2\sigma_y}\right) - \left(1 + \left(q_3 f^*\right)^2\right) = 0 \tag{2}$$

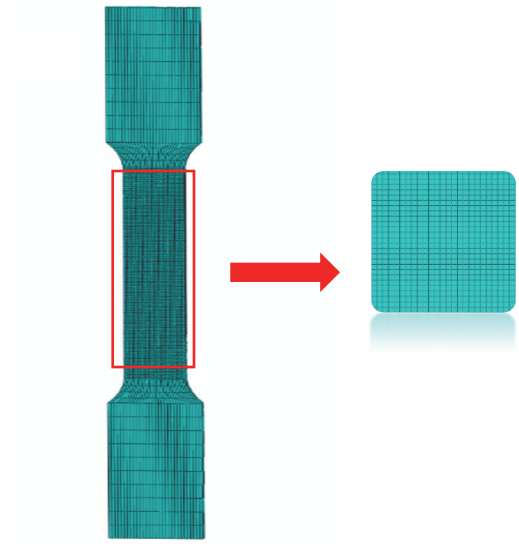

Figure 4: Finite element simulation model uniaxial test.

In Nahshon and Hutchinson's shear damage equations, σ_y is the yield stress, q is the Von Misses equivalent stress, p is the hydrostatic pressure, f * is the effective void volume fraction, and q1 to q3 are constants and dependent on the material's properties[49]:

$$f^*(f) = \begin{cases} f & f \le f_c \\ f_c + \dfrac{1/q1 - f_c}{f_f - f_c}(f - f_c) & f_c < f \end{cases} \tag{3}$$

$$\dot{f}_s = k_\omega f \omega(\sigma_{ij}) \frac{S_{ij}\dot{\varepsilon}_{ij}^p}{q} \tag{4}$$

$$\dot{f}_g = (1 - f)\dot{\varepsilon}^p \tag{5}$$

$$\dot{f}_n = A\frac{S_{ij}\dot{\varepsilon}_{ij}^p}{q} \tag{6}$$

$$A=\begin{cases}\dfrac{f_N}{s_N\sqrt{2\pi}}\exp\left[-\dfrac{1}{2}\left(\dfrac{\bar{\varepsilon}_m^p-\varepsilon_N}{s_N}\right)^2\right] & P\le 0\\ 0 & P>0\end{cases} \tag{7}$$

$$\dot{f}=\dot{f}_g+\dot{f}_n+\dot{f}_s \tag{8}$$

where k_ω is introduced as a new material parameter for the void nucleation rate of damage in pure shear conditions, $\omega(\sigma)$ is the stress- function used by Nahshon and Hutchinson, S is the deviatoric stress tensor and $\dot{\varepsilon}^p$ plastic strain rate tensor, f_c is the critical volume fraction of voids and f_f is the volume fraction of the void at the fractured moment This function is between the zero and one value, which for the axial stress state is zero and for the shear stress condition is one. Also, the $\dot{f}$ is rate of change in the voids volume fraction, $\dot{f}_g$ is the void growth, $\dot{f}_n$ is the nucleation rate, and $\dot{f}_s$ is the shear rate of the voids.

The VUMAT subroutine is implemented to utilize the modified GTN damage behavior of the material in Abaqus software. In this process stress tensor and internal state variables must be updated in the end of each increment If plastic state occurs the plastic corrections must be calculated. The corrections for Δεp (volumetric plastic strain increment) and Δεq (deviatoric plastic strain increment) are calculated using the Newton-Raphson iteration method. This iterative process helps refine the values of cp and cq, which are the corrections required for updating the internal variables. By iteratively adjusting these corrections, the algorithm achieves an accurate and reliable update of the stress tensor and internal state variables. The pseudo-code algorithm for developing the user subroutine is provided in Tab. 4 [38].

Initiate the stress tensor and internal variables at $t=0$ time.

Calculate elastic predictor $\sigma_{t+\Delta t}^T, p_{t+\Delta t}^T, q_{t+\Delta t}^T$:

$$\boldsymbol{\sigma}^T=\boldsymbol{\sigma}_t+\boldsymbol{C}^e:\Delta\boldsymbol{\varepsilon}\ ;\quad p^T=-\frac{1}{3}\boldsymbol{\sigma}^T:\boldsymbol{I}\ ;\quad q^T=\sqrt{\frac{3}{2}\boldsymbol{s}^T:\boldsymbol{s}^T} \tag{9-11}$$

Calculate the value of the yield function:

$$F_2=\Phi(p^T,q^T,\left(\bar{\varepsilon}_m^p\right)_t,\ f_t,\left(D_s\right)_t) \tag{12}$$

IF $F_2\ge 0$ then

k=0

While $|F_1|>$ tolerance or $|F_2|>$ tolerance do

Calculate the corrections c_p and c_q to update the $\Delta\varepsilon_p$ and $\Delta\varepsilon_q$ values:

$$\begin{cases}\left(\dfrac{\partial F_1}{\partial\Delta\varepsilon_p}\right)_{t+\Delta t}^k c_p+\left(\dfrac{\partial F_1}{\partial\Delta\varepsilon_q}\right)_{t+\Delta t}^k c_q=-\left(F_1\right)_{t+\Delta t}^k\\ \left(\dfrac{\partial F_2}{\partial\Delta\varepsilon_p}\right)_{t+\Delta t}^k c_p+\left(\dfrac{\partial F_2}{\partial\Delta\varepsilon_q}\right)_{t+\Delta t}^k c_q=-\left(F_2\right)_{t+\Delta t}^k\end{cases};\quad \begin{cases}\left(\Delta\varepsilon_p\right)_{t+\Delta t}^{k+1}=\left(\Delta\varepsilon_p\right)_{t+\Delta t}^k+c_p\\ \left(\Delta\varepsilon_q\right)_{t+\Delta t}^{k+1}=\left(\Delta\varepsilon_q\right)_{t+\Delta t}^k+c_q\end{cases};\quad \begin{cases}p_{t+\Delta t}^{k+1}=p^T+K\left(\Delta\varepsilon_p\right)_{t+\Delta t}^{k+1}\\ q_{t+\Delta t}^{k+1}=q^T-3G\left(\Delta\varepsilon_q\right)_{t+\Delta t}^{k+1}\end{cases} \tag{13-15}$$

Check the yield condition:

$$\left(F_1\right)_{t+\Delta t}^{k+1}=(\Delta\varepsilon_p)_{t+\Delta t}^{k+1}\left(\frac{\partial\Phi}{\partial q}\right)_{t+\Delta t}^{k+1}+(\Delta\varepsilon_q)_{t+\Delta t}^{k+1}\left(\frac{\partial\Phi}{\partial p}\right)_{t+\Delta t}^{k+1};\quad \left(F_2\right)_{t+\Delta t}^{k+1}=\Phi\left(p_{t+\Delta t}^{k+1},q_{t+\Delta t}^{k+1},\left(\bar{\varepsilon}_m^p\right)_{t+\Delta t}^{k+1},\ f_{t+\Delta t}^{k+1},\left(D_s\right)_{t+\Delta t}^{k+1}\right) \tag{16,17}$$

k = k + 1

End while

Update the stresses and state variables $\boldsymbol{\sigma}_{t+\Delta t}, \left(\bar{\varepsilon}_m^p\right)_{t+\Delta t}, f_{t+\Delta t}, \left(D_s\right)_{t+\Delta t}$:

$$\left(D_s\right)_{t+\Delta t} = \left(D_s\right)_{t+\Delta t}^{k+1}; \quad \left(\bar{\varepsilon}_m^p\right)_{t+\Delta t} = \left(\bar{\varepsilon}_m^p\right)_{t+\Delta t}^{k+1}; \quad f_{t+\Delta t} = f_{t+\Delta t}^{k+1}; \quad \boldsymbol{\sigma}_{t+\Delta t} = p_{t+\Delta t}^{k+1}\boldsymbol{I} + \frac{2}{3}q_{t+\Delta t}^{k+1}\boldsymbol{n} \quad (18\text{-}21)$$

Else

$$\left(\bar{\varepsilon}_m^p\right)_{t+\Delta t}^{k+1} = \left(\bar{\varepsilon}_m^p\right)_t; \quad f_{t+\Delta t}^{k+1} = f_t; \quad \left(D_s\right)_{t+\Delta t}^{k+1} = \left(D_s\right)_t; \quad \boldsymbol{\sigma}_{t+\Delta t} = \boldsymbol{\sigma}^T \quad (22\text{-}25)$$

End if

Table 4: Pseudo-code for implementation of the plasticity and damage modelling.

Tab. 5 presents the impact of nine variations of the modified GTN parameters on the maximum force and fracture displacement, as determined through finite element (FE) simulations using 36 samples. These variations of the GTN parameters were used as input data for the ANN modeling. The nine parameters, which are part of the constitutive equation of the modified GTN model, were incorporated into the ANN algorithm to predict the maximum force and fracture displacement. By analyzing the relationship between these modified GTN parameters and the mechanical response of the samples obtained from FE simulations, the ANN model offers a valuable tool for accurately predicting the maximum force and fracture displacement in the context of the modified GTN model. This information can be crucial for understanding the fracture behavior of materials and optimizing their performance in various engineering applications. These parameters include constitutive parameter (q1, q2), initial void volume fraction (f0), critical void volume fraction (fc), void volume fraction at failure (ff), the void volume fraction of nucleated voids (Fn), the standard deviation of the distribution (Sn), and the mean value of the nucleation strain (En), and shear coefficient (kW).

	Inputs									Outputs	
NO	q 1	q 2	f 0	f c	f_f	S n	f n	E n	K w	Fmax	FD
1	1	0.75	0	0.005	0.01	0.1	0.01	0.1	0	5796.624	0.656477
2	1.5	0.75	0	0.005	0.01	0.1	0.01	0.1	0	5795.857	0.646894
3	1	1	0	0.005	0.01	0.1	0.01	0.1	0	5796.553	0.650822
						…….					
34	1	0.932651	0.004269	0.005	0.019845	0.138969	0.059868	0.140231	18.87184	5735.889	0.366438
35	1	0.896648	0.004499	0.005	0.051262	0.134238	0.046769	0.176476	22.52134	5756.132	0.424102
36	1	0.918501	0.004384	0.005	0.026097	0.1336	0.039757	0.166472	12.12199	5763.917	0.444408

Table 5: The modified GTN parameter, maximum force, and fracture displacement data train ANN.

ANN MODELLING

An ANN is a computational model composed of interconnected artificial neurons trained on input data to perform a specific task. In this study, the ANN is utilized as an efficient tool for network classification by combining multiple hidden layers and a training function. The Levenberg-Marquardt [50] algorithm is used to train the ANN, which involves computing the outputs of the neurons and applying an activation function to the summation of input data and neuron weights. The hidden layer neurons use the hyperbolic tangent activation function, while the output layer neurons use the linear activation function. The sample data is randomly split into three sections, with 70% used for training, 15% for testing, and 15% for validation. The ANN design consists of N-layer networks with 1 to 3 hidden layers and variable neurons ranging from 1 to 22. Each hidden layer is evaluated independently, and multiple training sets are tested for each set of neurons to obtain the best-predicted model. This process is repeated for each hidden layer to determine the optimal

configuration for the ANN. It is important to note that different training data sets can affect the accuracy of the net and the resulting predictions, so multiple sets are trained to ensure the best possible results.

The R-squared correlation (R^2) parameter is calculated to evaluate the neural network's performance and results. A higher value of R^2 indicates a more accurate prediction by the network, with a value closer to 1 being desirable. In this study, the nine GTN parameters are selected as input parameters to capture the complex effects of these parameters on the fracture behavior of materials. The neural network is trained to predict the maximum force (Fmax) and fracture displacement (FD), which serve as the output parameters. These predicted values are then compared to experimental results to verify the accuracy of the neural network's predictions. By using these input and output parameters, the neural network aims to provide an effective tool for understanding and predicting the fracture behavior of materials.

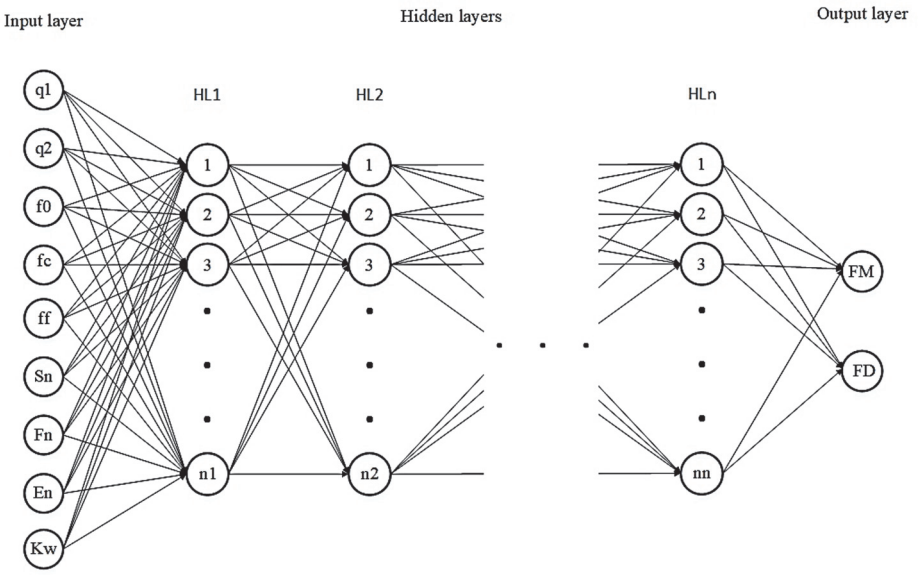

Figure 5: Designed N-layer network [42].

The relative influence of each variable is determined by evaluating the calibrated connection weights using the Connection Weights (CW) methodology. In this investigation, other commonly used methods like the Garson algorithm, which have been found to be less effective, are not considered. Each parameter's Relative Importance (RI) can be analyzed by examining the obtained connection weights in the neural network [51].

The CW algorithm utilizes the sum of products for all weights connecting the input and hidden neurons, as well as the weights between the hidden layer and output neurons. By calculating these connection weights, we can assess the relative importance of each parameter in influencing the neural network's output.

$$RI_I = \sum w_{In_1} w_{n_1 n_2} \dots w_{n_n o} \tag{26}$$

The relative importance (RI) of an input variable, represented as "I", is determined by summing the products of the corresponding weights (w) connecting the input layer neurons (I) with the hidden layer neurons (n) and the hidden layer neurons with the output neurons (o). In other words, the RI is calculated by multiplying the weights along the pathways from the input layer to the output layer and summing these products. This process allows us to assess the relative importance of the input variable I in influencing the output of the neural network.

MICROSTRUCTURE

Fig. 6 shows the microstructures of Ti6Al4V sample manufactured by the SLM process. The samples were prepared using standard metallurgical processes for microstructural analysis. The samples were then polished using 0.05 µm colloidal silica and etched using Kroll's reagent, which consisted of 2 vol% hydrofluoric acid and 3 vol% nitric acid

in distilled water. It is found that prior-β grains have acicular α-laths; however, these prior-β grains are elongated and cross build layers.

In addition, a scanning electron microscope (SEM) examination was carried out on the pieces in order to gain insight into the fracture surface. After that, the produced samples were inspected using a MIRA3 TESCAN optical microscope in order to capture pictures for a later examination at the grain level.

Ductile fracture in the SLM of Ti6Al4V is shown by the finer ductile dimples at the tensile fracture surface. The specimen fracture surfaces, as seen by Fig. 7, displays fracture surfaces with smoother cup and cone characteristics and a large population of finer dimples. There is a great deal of friction between the fracture surfaces on top and below. Failure occurs without significant plastic deformation, resulting in smooth, curved conchoidal fracture surfaces dominated by the void shear mechanism. The presence of severe friction between upper and lower fracture surfaces further emphasizes the intricate interplay of mechanical factors.

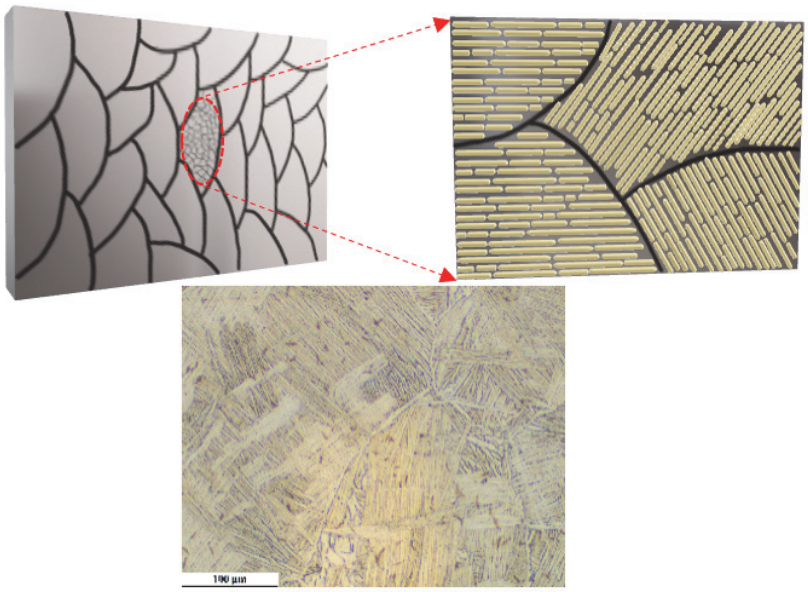

Figure 6: Micrographs of Ti-6Al-4V specimen manufactured by SLM process.

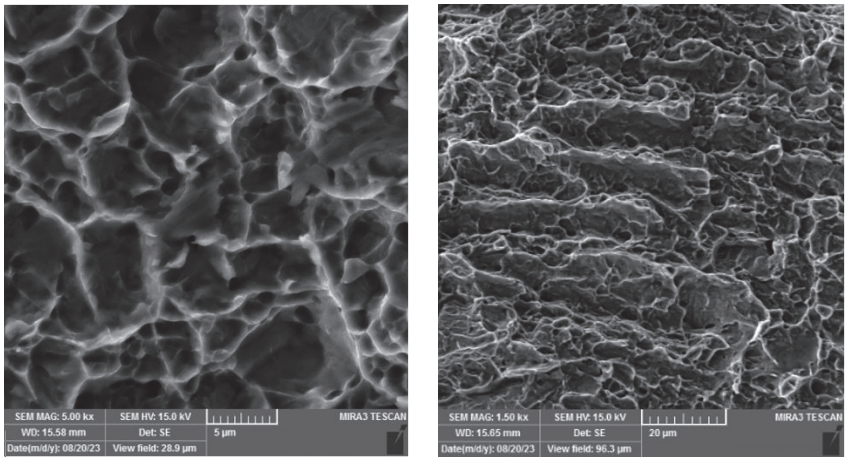

Figure 7: A representative fracture surface of the specimen.

RESULTS AND DISCUSSION

The effect of the number of neurons on the prediction accuracy of the relationship between parameters is investigated in this study. The neural network is trained using three different hidden layers, with each layer containing a varying number of neurons from 1 to 22. The results for two output parameters are shown in Figs. 8, 9, and 10, corresponding to each hidden layer.

Based on the obtained results, it is observed that three hidden layers provide the most suitable and accurate prediction closest to the experimental test. It is also found that fewer neurons are sufficient for predicting the maximum force, indicating that there are simpler relationships among the parameters that lead to better results.

However, it should be noted that while adding a hidden layer improves the accuracy of the predicted results, it does not necessarily imply that increasing the number of hidden layers will always yield better outcomes. In the case of predicting the maximum force, fewer neurons are needed to achieve accurate results. Therefore, the optimal number of hidden layers and neurons depends on the predicted output parameter and the complexity of the underlying relationships among the parameters.

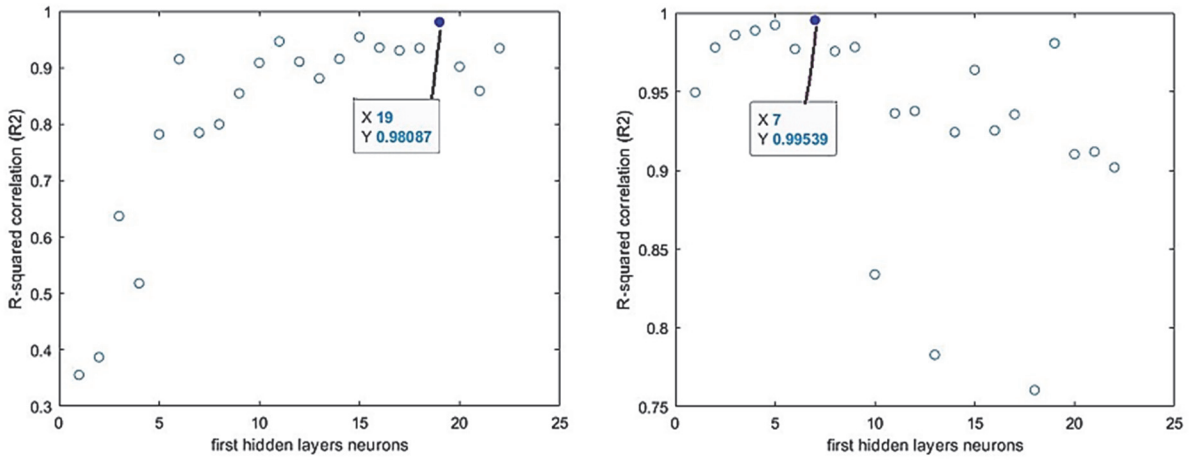

Figure 8: (a) Fracture displacement (b) Maximum force one layer.

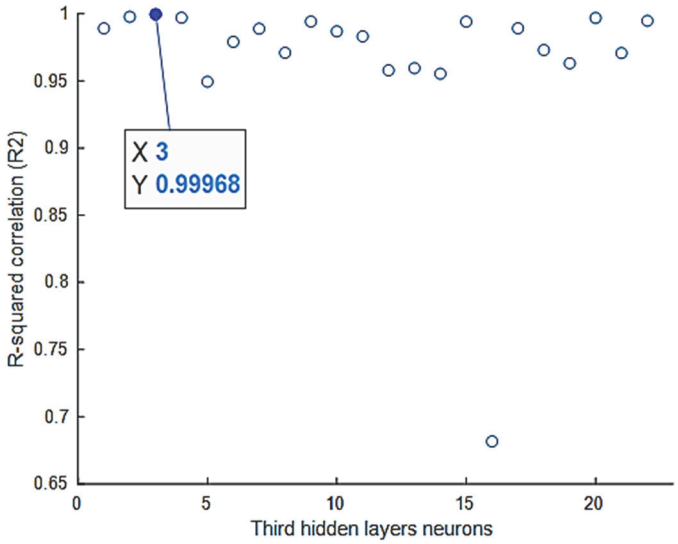

Figure 9: Maximum force three-layers (First layer 4, second layer 17).

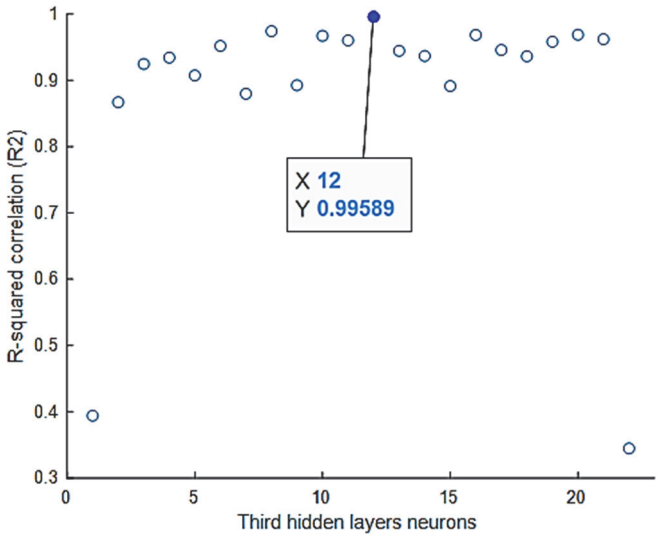

Figure 10: Fracture displacement three-layers (First layer 16, second layer 14).

Based on the results presented in Figs. 8-10, the best predictions for maximum force are achieved with a correlation coefficient (R^2) of 0.99539 using one hidden layer with seven neurons, 0.99947 using two hidden layers with nineteen neurons in the first layer and six neurons in the second layer, and 0.999678 using three hidden layers with four neurons in the first layer, seventeen neurons in the second layer, and three neurons in the third layer. For fracture displacement prediction, the best results are obtained with R^2 values of 0.98087 using nineteen neurons in one hidden layer, 0.99125 using two hidden layers with nine neurons in the first layer and twelve neurons in the second layer, and 0.995895 using three hidden layers with sixteen neurons in the first layer, fourteen neurons in the second layer, and twelve neurons in the third layer. Fig. 11 demonstrates that increasing the number of hidden layers leads to improved results and significantly increases the optimization time. Therefore, predicting the maximum force using fewer hidden layers is logical, considering the simpler relationships involved. On the other hand, due to the complexity of the relationships between GTN parameters and fracture displacement, employing more hidden layers yields better results and achieves a suitable R^2 correlation Coefficient.

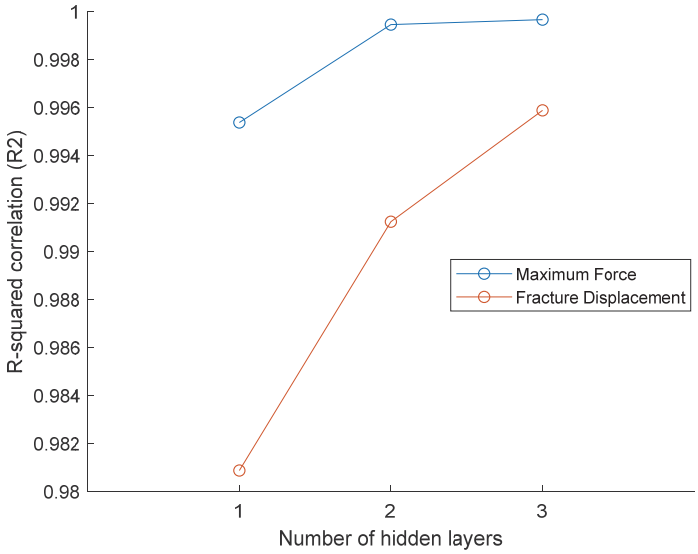

Figure 11: Effect of the number of layers on R^2 -value accuracy.

The CW algorithm determined the relative importance of each input variable based on calibrated connection weights. In summary, the analysis presented in Fig. 12 reveals that the parameter (f_0), representing the initial porosity of the material, has a dominant influence on fracture displacement. On the other hand, the parameter (q_1) exhibits a lower influence on

fracture displacement. Moreover, the findings suggest that a three-layer ANN demonstrates a higher relative influence on general fracture displacement. It is important to note that the differences in the correlation between input and output parameters across various layers are attributed to the variations in the weights within each layer, which ultimately affect the prediction of results. However, the analysis indicates that three parameters, namely f_0, Kw, and f_c, have a dominant influence on the maximum force. Conversely, the parameters En and fn exhibit a lower influence on the maximum force. Additionally, the findings suggest that an ANN with various layers does not have a significant relative influence on the general maximum force.

However, it should be noted that ff and En also affect both fracture surface appearance and energy prediction, thus warranting additional consideration in this study.

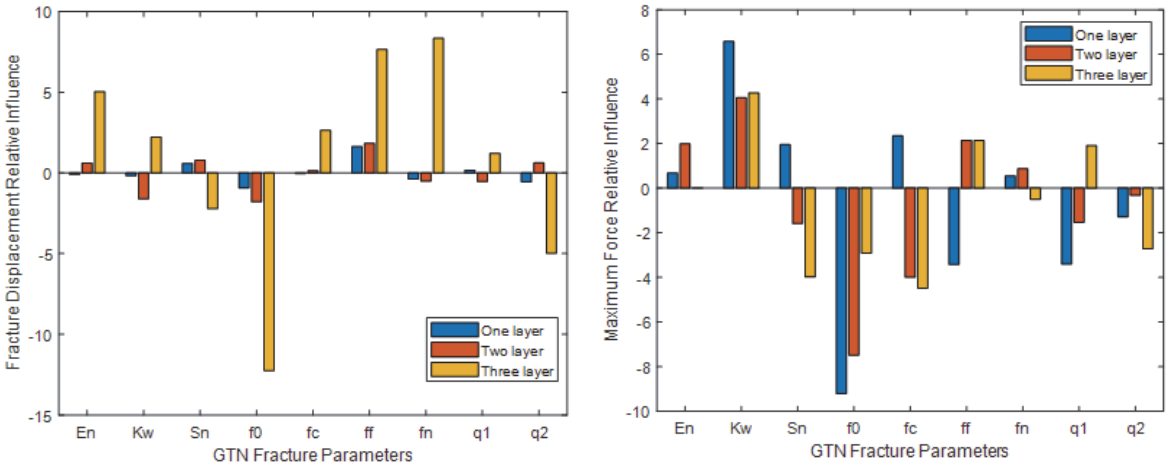

(a) (b)

Figure 12: Relative influence of various layers of the material-dependent GTN parameters on (a) fracture displacement (b) maximum force.

Furthermore, in Figs. 13 and 14, the accuracy of predictions from various layers of the ANN is compared to the results obtained from finite element simulations. It is evident that all layers of the ANN exhibit consistent and reliable results that align well with the finite element method. Notably, the third layer of the ANN demonstrates higher accuracy compared to the other layers when compared to the finite element simulations.

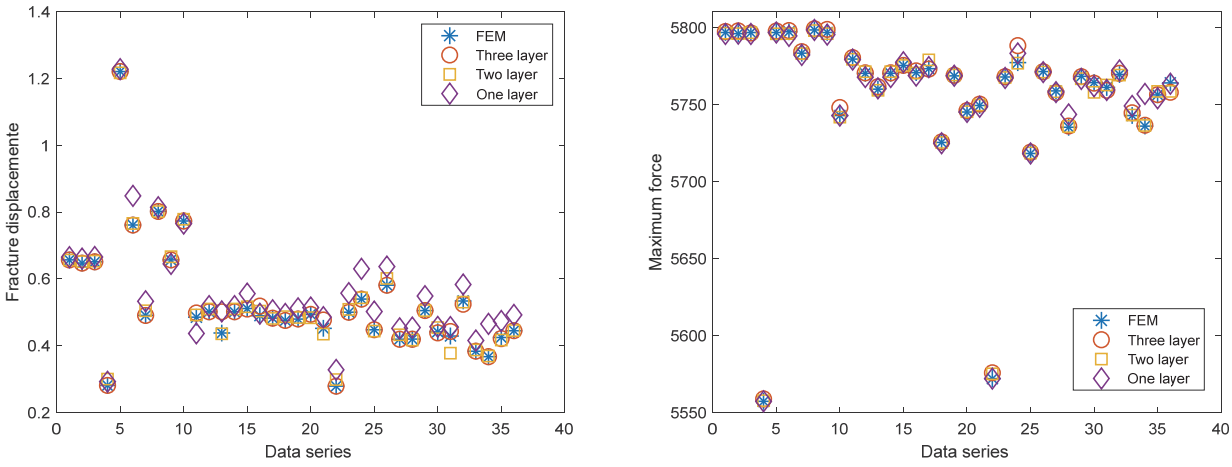

(a) (b)

Figure 13: The comparison of finite element simulation and predicted results by various layers. (a) fracture displacement (b) maximum force.

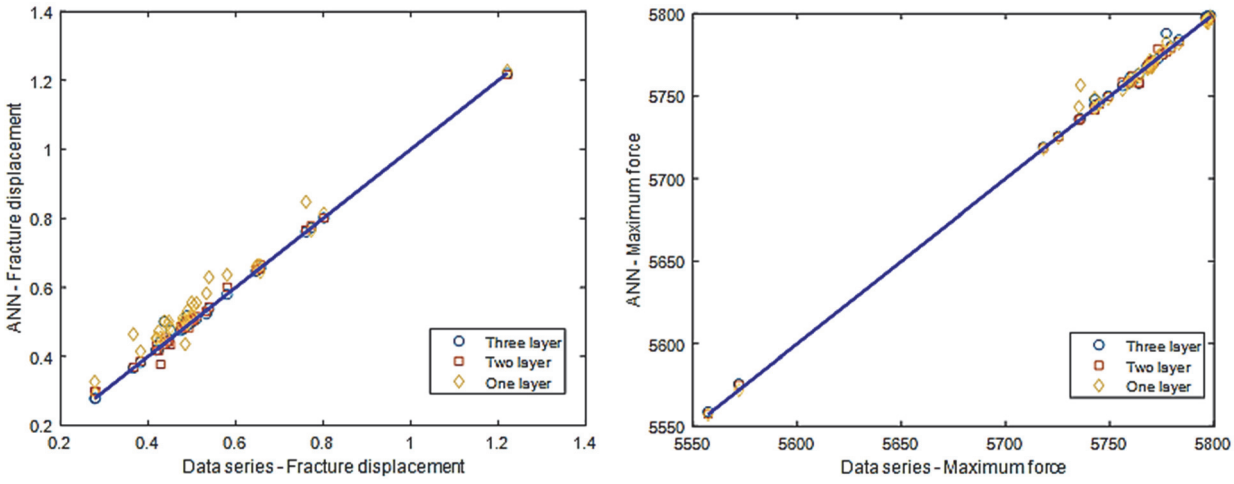

(a) (b)

Figure 14: The results of performance R^2 for various layers. (a) Fracture displacement (b) Maximum force

CONCLUSIONS

The study investigated the impact of the number of layers and neurons on the accuracy of an ANN in predicting the fracture behavior and the relative influence of various GTN parameters on fracture displacement and maximum force of Ti6Al4V alloys in the SLM process.

The ANN was found to be a suitable method for determining the GTN fracture model coefficient, with significant influence from the number of hidden layers and the choice of training function on the accuracy of predictions.

Increasing the number of layers and neurons in the ANN led to improved accuracy in predicting fracture displacement, which is influenced by complex relationships among the GTN parameters.

For predicting maximum force, a lesser number of hidden layers still resulted in acceptable accuracy, although higher layers also provided accurate results.

It is recommended to use an ANN with more hidden layers and neurons when forecasting fracture displacement, while for maximum force prediction, a network with fewer hidden layers can still achieve satisfactory accuracy.

The investigation examined the relative influence of different layers and material- dependent GTN parameters on fracture displacement and maximum force. The results indicate that f_0, representing a specific GTN parameter, has the most significant effect on both fracture displacement and maximum force. This finding suggests that f_0 plays a crucial role in determining these two mechanical properties.

However, it should be noted that increasing the number of layers and neurons also leads to longer optimization times, which should be considered in practical applications.

DISCLOSURE STATEMENT

No potential conflict of interest was reported by the author(s).

REFERENCES

[1] DebRoy, T., Wei, H.L., Zuback, J.S., Mukherjee, T., Elmer, J.W., Milewski, J.O., Beese, A.M., Wilson-Heid, A.D., De, A. and Zhang, W., (2018). Additive manufacturing of metallic components–process, structure and properties. Progress in Materials Science, 92, pp.112-224.

[2] Majeed, A., Ahmed, A., Lv, J., Peng, T. and Muzamil, M., (2020). A state-of-the-art review on energy consumption and quality characteristics in metal additive manufacturing processes. Journal of the Brazilian Society of Mechanical Sciences and Engineering, 42, pp.1-25.

[3] Patel, A. and Taufik, M., (2024). Extrusion-based technology in additive manufacturing: a comprehensive review. Arabian Journal for Science and Engineering, 49(2), pp.1309-1342.

[4] Behvar, A. and Haghshenas, M., (2023). A critical review on very high cycle corrosion fatigue: Mechanisms, methods, materials, and models. Journal of space safety engineering.

[5] Mahtabi, M., Yadollahi, A., Stokes, R., Morgan-Barnes, C., Young, J., Doude, H. and Bian, L., 2022. Effect of powder reuse on microstructural and fatigue properties of Ti-6Al-4V fabricated via directed energy deposition.

[6] Ltjering, G., and Williams, J. C. (2007). Titanium, Engineering materials and processes.

[7] Babakan, A. M., Davoodi, M., Shafaie, M., Sarparast, M., and Zhang, H. (2023). Predictive modeling of porosity in AlSi10Mg alloy fabricated by laser powder bed fusion: A comparative study with RSM, ANN, FL, and ANFIS. The International Journal of Advanced Manufacturing Technology, 129(3), pp.1097-1108.

[8] Mahtabi, M., Yadollahi, A., Ataollahi, S., and Mahtabi, M. J. (2023). Effect of build height on structural integrity of Ti-6Al-4V fabricated via laser powder bed fusion. Engineering Failure Analysis, 154, 107691.

[9] Mahtabi, M., Yadollahi, A., Stokes, R., Doude, H., and Priddy, M. (2023). Effect of build interruption during laser powder bed fusion process on structural integrity of Ti-6Al-4V. Engineering Failure Analysis, 153, 107626.

[10] Mahtabi, M., Yadollahi, A., Stokes, R., Doude, H., and Priddy, M. Effect of Build Interruption During Laser Beam Powder Bed Fusion Process on Structural Integrity of Ti-6al-4v. Available at SSRN 4459402.

[11] Bergo, S., Morin, D., Børvik, T., and Hopperstad, O. S. (2021). Micromechanical modelling of ductile fracture in pipeline steel using a bifurcation-enriched porous plasticity model. International Journal of Fracture, 227, pp.57-78.

[12] Gholipour, H., Biglari, F. R., and Nikbin, K. (2019). Experimental and numerical investigation of ductile fracture using GTN damage model on in-situ tensile tests. International Journal of Mechanical Sciences, 164, 105170.

[13] Hancock, J. W., and Mackenzie, A. C. (1976). On the mechanisms of ductile failure in high-strength steels subjected to multi-axial stress-states. Journal of the Mechanics and Physics of Solids, 24(2-3), pp.147-160.

[14] Rice, J. R., and Tracey, D. M. (1969). On the ductile enlargement of voids in triaxial stress fields∗. Journal of the Mechanics and Physics of Solids, 17(3), pp.201-217.

[15] McClintock, F. A. (1968). A criterion for ductile fracture by the growth of holes.

[16] Behvar, A., Eftekhary, H., Cheraghi, A., and Adazbeh, M. (2018). Microscopic illustration of zinc evaporation and ZnO nanowire production during brass alloy sintering. Int J Eng Technol, 10(4), pp.932-941.

[17] Gurson, A. L. (1977). Continuum theory of ductile rupture by void nucleation and growth: Part I—Yield criteria and flow rules for porous ductile media.

[18] Tvergaard, V., and Needleman, A. (1984). Analysis of the cup-cone fracture in a round tensile bar. Acta metallurgica, 32(1), pp.157-169.

[19] Wilson-Heid, A. E., Furton, E. T., and Beese, A. M. (2021). Contrasting the role of pores on the stress state dependent fracture behavior of additively manufactured low and high ductility metals. Materials, 14(13), 3657.

[20] El Khatib, O., Hütter, G., Pham, R. D., Seupel, A., Kuna, M., and Kiefer, B. (2023). A non-iterative parameter identification procedure for the non-local Gurson–Tvergaard–Needleman model based on standardized experiments. International Journal of Fracture, 241(1), pp.73-94.

[21] Sarparast, M., Shafaie, M., Babakan, A.M., Davoodi, M. and Zhang, H., (2023). Investigation of ANN structure on predicting the fracture behavior of additively manufactured Ti-6Al-4V alloys.

[22] Zhang, W.W., Wang, X.S., Cui, X.L. and Yuan, S.J., (2015). Analysis of corner filling behavior during tube hydro-forming of rectangular section based on Gurson–Tvergaard–Needleman ductile damage model. Proceedings of the Institution of Mechanical Engineers, Part B: Journal of Engineering Manufacture, 229(9), pp.1566-1574.

[23] Saha, S., Gupta, K. K., Maity, S. R., & Dey, S. (2022). Data-driven probabilistic performance of Wire EDM: A machine learning based approach. Proceedings of the Institution of Mechanical Engineers, Part B: Journal of Engineering Manufacture, 236(6-7), 908-919.

[24] Prieto, A., Prieto, B., Ortigosa, E.M., Ros, E., Pelayo, F., Ortega, J. and Rojas, I., (2016). Neural networks: An overview of early research, current frameworks and new challenges. Neurocomputing, 214, pp.242-268.
[25] Nartu, M.S.K.K.Y., Dasari, S., Sharma, A., Mantri, S.A., Sharma, S., Pantawane, M.V., McWilliams, B., Cho, K., Dahotre, N.B. and Banerjee, R., (2021). Omega versus alpha precipitation mediated by process parameters in additively manufactured high strength Ti–1Al–8V–5Fe alloy and its impact on mechanical properties. Materials Science and Engineering: A, 821, p.141627.
[26] Tsai, K.M. and Luo, H.J., (2017). An inverse model for injection molding of optical lens using artificial neural network coupled with genetic algorithm. Journal of Intelligent Manufacturing, 28, pp.473-487.
[27] Wang, F., Zhao, J. and Zhu, N., (2016). Constitutive equations and ANN approach to predict the flow stress of Ti-6Al-4V alloy based on ABI tests. Journal of Materials Engineering and Performance, 25, pp.4875-4884.
[28] Nimbagal, V., Banapurmath, N.R., Sajjan, A.M., Patil, A.Y. and Ganachari, S.V., (2021). Studies on hybrid bio-nanocomposites for structural applications. Journal of Materials Engineering and Performance, 30(9), pp.6461-6480.
[29] Maleki, E., Bagherifard, S. and Guagliano, M., (2021). Application of artificial intelligence to optimize the process parameters effects on tensile properties of Ti-6Al-4V fabricated by laser powder-bed fusion. International Journal of Mechanics and Materials in Design, pp.1-24.
[30] Wang, C., Tan, X.P., Tor, S.B. and Lim, C.S., (2020). Machine learning in additive manufacturing: State-of-the-art and perspectives. Additive Manufacturing, 36, p.101538.
[31] Chinchanikar, S., Shinde, S., Gaikwad, V., Shaikh, A., Rondhe, M. and Naik, M., (2022). ANN modelling of surface roughness of FDM parts considering the effect of hidden layers, neurons, and process parameters. Advances in Materials and Processing Technologies, pp.1-11.
[32] Mehrpouya, M., Gisario, A., Nematollahi, M., Rahimzadeh, A., Baghbaderani, K.S. and Elahinia, M., (2021). The prediction model for additively manufacturing of NiTiHf high-temperature shape memory alloy. Materials today communications, 26, p.102022.
[33] Jimenez-Martinez, M., and Alfaro-Ponce, M. (2021). Effects of synthetic data applied to artificial neural networks for fatigue life prediction in nodular cast iron. Journal of the Brazilian Society of Mechanical Sciences and Engineering, 43(1), p.10.
[34] Trivedi, P., Vansjalia, R., Erra, S., Narayanan, S. and Nagaraju, D., (2023). A fuzzy CRITIC and fuzzy WASPAS-based integrated approach for wire arc additive manufacturing (WAAM) technique selection. Arabian Journal for Science and Engineering, 48(3), pp.3269-3288.
[35] Popovich, A., Sufiiarov, V., Borisov, E. and Polozov, I.A., (2015). Microstructure and mechanical properties of Ti-6Al-4V manufactured by SLM. Key Engineering Materials, 651, pp.677-682.
[36] Kumar, S.L., Aravind, H.B. and Hossiney, N., (2019). Digital image correlation (DIC) for measuring strain in brick masonry specimen using Ncorr open source 2D MATLAB program. Results in Engineering, 4, p.100061.
[37] Butler, D. and Woolliams, P., (2020). Standards in additive manufacturing. In Precision Metal Additive Manufacturing (pp. 133-156). CRC Press.
[38] Wilson-Heid, A. E. (2021). Additively Manufactured Metals: Effect of Microstructure and Defects on Multiaxial Plasticity and Fracture Behavior. The Pennsylvania State University.
[39] Wilson-Heid, A.E., Wang, Z., McCornac, B. and Beese, A.M., (2017). Quantitative relationship between anisotropic strain to failure and grain morphology in additively manufactured Ti-6Al-4V. Materials Science and Engineering: A, 706, pp.287-294.
[40] V. MATLAB, 9.6. 0.1072779 (R2019a), The MathWorks Inc.: Natick, MA, USA.
[41] Needleman, A. and Tvergaard, V., (1992). Analyses of plastic flow localization in metals.
[42] Shafaie, M., Khademi, M., Sarparast, M. and Zhang, H., (2022). Modified GTN parameters calibration in additive manufacturing of Ti-6Al-4 V alloy: a hybrid ANN-PSO approach. The International Journal of Advanced Manufacturing Technology, 123(11), pp.4385-4398.
[43] F. Abaqus, (2014), Dassault systemes simulia corporation, Providence, Rhode Island, USA.
[44] Barfeh, A., Hashemi, R., Safdarian, R., Rahmatabadi, D., Aminzadeh, A. and Sattarpanah Karganroudi, S., (2023). Predicting the forming limit diagram of the fine-grained AA 1050 sheet using GTN damage model with experimental verifications. Proceedings of the Institution of Mechanical Engineers, Part B: Journal of Engineering Manufacture, 237(14), pp.2325-2335.
[45] Lutz, M. (2001). Programming python. " O'Reilly Media, Inc.".

[46] Mirnia, M.J. and Shamsari, M., (2017). Numerical prediction of failure in single point incremental forming using a phenomenological ductile fracture criterion. Journal of Materials Processing Technology, 244, pp.17-43.
[47] Needleman, A. and Tvergaard, V.F., (1984). An analysis of ductile rupture in notched bars. Journal of the Mechanics and Physics of Solids, 32(6), pp.461-490.
[48] Tvergaard, V., (1989). Material failure by void growth to coalescence. Advances in applied Mechanics, 27, pp.83-151.
[49] Sun, Q., Lu, Y. and Chen, J., (2020). Identification of material parameters of a shear modified GTN damage model by small punch test. International Journal of Fracture, 222, pp.25-35.
[50] Pujol, J., (2007). The solution of nonlinear inverse problems and the Levenberg-Marquardt method. Geophysics, 72(4), pp.W1-W16.
[51] Paermentier, B., Debruyne, D. and Talemi, R., (2021). A machine learning based sensitivity analysis of the GTN damage parameters for dynamic fracture propagation in X70 pipeline steel. International Journal of Fracture, 227(1), pp.111-132.